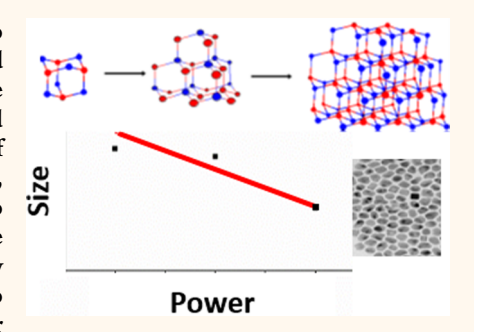
# Microwave Enhancement of Autocatalytic **Growth of Nanometals**

Bridgett Ashley, †,‡ Parth N. Vakil,† Brian B. Lynch,§ Christopher M. Dyer,† Joseph B. Tracy,§ [o] Jeffery Owens,‡ and Geoffrey F. Strouse\*,† [o]

Supporting Information

Downloaded via FLORIDA STATE UNIV on April 25, 2019 at 17:26:18 (UTC). See https://pubs.acs.org/sharingguidelines for options on how to legitimately share published articles.

ABSTRACT: The desire for designing efficient synthetic methods that lead to industrially important nanomaterials has led a desire to more fully understand the mechanism of growth and how modern synthetic techniques can be employed. Microwave (MW) synthesis is one such technique that has attracted attention as a green, sustainable method. The reports of enhancement of formation rates and improved quality for MW driven reactions are intriguing, but the lack of understanding of the reaction mechanism and how coupling to the MW field leads to these observations is concerning. In this manuscript, the growth of a metal nanoparticles (NPs) in a microwave cavity is spectroscopically analyzed and compared with the classical autocatalytic method of NP growth to elucidate the underpinnings for the observed enhanced growth behavior for



metal NPs prepared in a MW field. The study illustrates that microwave synthesis of nickel and gold NPs below saturation conditions follows the Finke-Watzky mechanism of nucleation and growth. The enhancement of the reaction arises from the size-dependent increase in MW absorption cross section for the metal NPs. For Ni, the presence of oxides is considered via theoretical computations and compared to dielectric measurements of isolated nickel NPs. The study definitively shows that MW growth can be modeled by an autocatalytic mechanism that directly leads to the observed enhanced rates and improved quality widely reported in the nanomaterial community when MW irradiation is employed.

KEYWORDS: microwave, autocatalytic, mechanism, spectroscopy, nanoparticle, nickel, core/shell

he early days of nanoscience were focused on developing efficient synthetic methods, including hot injection, microwave, microfluidic, and use of single source precursors. Since then the nanoscience field has matured with a growing focus on understanding the growth mechanisms for nanocrystals and how the reaction can be controlled via heating and precursor addition.<sup>2-7</sup> Of the recently developed synthetic tools for reproducible preparation of nanomaterials, microwave (MW) heating techniques<sup>3-15</sup> have been purported to enhance nucleation and growth rates and produce improved material quality in II–VI, 5,6 III–V, 7,8 IV semiconductors and metals. 10,11,23,24 While there is no doubt of the claims, the rationale for enhancement has not been satisfactorily explained.

In nanometal growth in a MW, the reported enhanced reactions are poorly understood but clearly must reflect the absorption of the MW energy to produce heat, which is measurable by dielectric spectroscopy. There is no possibility that a single MW photon at 2.45 GHz can initiate a reaction; however, the absorption of the 2.45 GHz photon can produce heat via frictional processes. 12 In addition, the formation of nanometal under identical reaction conditions must follow the

well-defined thermodynamic and kinetic models for nanoparticle (NP) growth from a monomer. The growth behavior of NiNPs and AuNPs grown under mildly reducing conditions in a convective reaction has been fully developed and ascribed to an autocatalytic mechanism. <sup>13–15</sup> The autocatalytic mechanism for metal growth occurs under conditions where a M<sup>0</sup> monomer is formed far below saturation conditions due to a slow kinetic conversion of the metal coordination complex (precursor) to an active monomer step. This leads to a condition where the separation of nucleation and growth occur due to the rate of growth being faster than the rate of nucleation. Turkevich et al. 15 originally observed this behavior in AuNPs, which led to Finke et al. proposing an autocatalytic mechanism occurring through a series of steps.<sup>2</sup> More recently the autocatalytic theory was expanded to account for multiple steps in the reaction to explain the narrow size dispersity of materials. 16-18 The Finke-Watzky (F-W) mechanism for NP growth assumes activation of the precursor is kinetically slow,

Received: June 9, 2017 Accepted: October 2, 2017 Published: October 2, 2017

<sup>&</sup>lt;sup>†</sup>Department of Chemistry and Biochemistry, Florida State University; Tallahassee, Florida 32306-4390, United States

<sup>‡</sup>Air Force Civil Engineer Center, Tyndall Air Force Base, Panama City, Florida 32403, United States

<sup>&</sup>lt;sup>§</sup>Department of Materials Science and Engineering, North Carolina State University; Raleigh, North Carolina 27695, United States

while growth at a nuclear facet is energetically more favorable than formation of new nuclei. The autocatalytic mechanism is unlike the LaMer classical nucleation theory where super saturation is required to initiate burst nucleation and diffusion limited growth.

Since the earliest report of autocatalytic growth by Turkevich and defined by F-W, the autocatalytic mechanism has been validated for several transition metals, <sup>19,28–30</sup> including Ni, <sup>13</sup> and has even been expanded to describe several natural phenomena, including plaque formation in Alzheimer's disease. <sup>20</sup> Measuring the growth kinetics of a nanometal under MW reaction conditions and correlating the behavior with the predictive autocatalytic models can allow the MW enhancement to be understood and correlated to observation in convective reactions.

To interrogate the growth mechanism for metal NPs in mildly reducing solvents in a MW reactor and the influence of the MW field, the growth of NiNPs, and as a comparison to literature reported autocatalytic growth for AuNPs, 16,21 is analyzed. While AuNPs are well studied in the field due to plasmonic properties, NiNPs were chosen as a classical soft magnetic material that mechanistically has been studied in solvothermal reactions 13,22 and is an important material for applications in electromagnetic shielding and catalytic applications.<sup>23</sup> By correlating the MW power absorbed and the temperature of the reaction, it is demonstrated that the MWfacilitated growth of metal NP follows the F-W autocatalytic model.2 The data support a model wherein MW-induced growth enhancement is due to efficient energy coupling to the reactants, and sustained growth is due to MW absorption into the metal NP as it grows, resulting in uniform nucleation, accelerated NP growth, and thus narrower size dispersities. The results of this study are consistent with recent work by de la Hoz, 24,25 which showed that, for a chemical reaction in the MW, both the activation energy and MW absorption are important factors in determining that a reaction performed in a MW reactor will or will not improve noticeably when compared to a conventional lyothermal reaction. A theoretical framework comparing size and temperature response of metal NPs grown in a 2.45-GHz MW field can provide a context to understand the growth of nanometals in a MW cavity.

As part of the study, scaling law behavior for metal NP MW absorption is developed to elucidate the temperature- and sizedependent permittivity, permeability, and role of potential oxides at the surface on the NiNP during nucleation and growth. The permittivity and permeability data of the isolated Ni nanocrystals support the rapid formation of a native oxide layer (3 monolayers,  $\sim 1.2$  nm) on the surface following isolation of the Ni from the reaction and not during the reaction. The presence of a stable oxide that rapidly forms after isolation may answer a common question why NiNPs embedded in polymers to enhance EMI shielding exhibit reduced shielding until the percolation threshold is exceeded. The observation can be explained by the oxide contributions, as the experimental size-dependent dielectric data suggest that the presence of as little as a monolayer of oxide results in loss of the dielectric benefits of NiNP inclusion for EMI shielding.<sup>23,26</sup>

Although NiNP and AuNP are the only metal NPs fully explored in this manuscript, the insights can be extended to materials grown in a MW reactor when the precursor activation step is kinetically slow. By carrying out nanometal growth reactions in mildly reducing conditions, control of growth behavior can be achieved through power and concentration

even at conditions below supersaturation. The understanding of the MW growth behavior for a nanometal as merely a thermodynamic and kinetic problem allows the extension of MW methods to a much wider range of materials without invoking nonthermodynamic effects.

## **RESULTS AND DISCUSSION**

Size- and Temperature-Dependent MW Absorption. During the growth of a metal NP from a molecular precursor, the impingent MW energy is converted into heat through molecular motion driven by dipolar polarization of the solvent and precursors to initiate critical nuclei formation. As the precursor is consumed and the metal NP grows, the dipolar cross-section of the system will evolve. For a metal, MW coupling also includes ohmic losses, charge separation, and Maxwell—Wagner heating at the solution— metal interface, which enhances the MW heating. The contribution from the individual components will evolve with the size-dependent metallic properties of the growing metal NP. Additionally, solvent and vessel contributions, which vary with temperature and dielectric properties, must also be considered.

The complex dielectric is related to the absorption cross-section or the point at which the amplitude of the impinging MW field decreases by 1/e. The rate of decrease is proportional to the complex permittivity of a material,  $\varepsilon^* = \varepsilon' + i\varepsilon''$  and is frequency and temperature dependent. The complex dielectric includes a term for the ability of a material to store electrical charge—known as the permittivity and represented by  $\varepsilon'$ —and a term for the combined electronic losses (dipole, ionic, and Maxwell—Wagner) of a material, known as the loss factor, represented by  $\varepsilon''$ . For simplicity, MW chemists often use the term  $\tan \delta = \varepsilon''/\varepsilon'$  because the absorbed power  $(P_{\rm abs}) \propto \tan \delta$ . The rate of growth of the metal NP from the precursor will depend on  $P_{\rm abs}$  into the system (MW cavity, vessel, solvents, and precursors).  $P_{\rm abs}$  is related to the complex dielectric and the heat capacity, such that

$$P_{\rm abs} = MC_p \frac{\Delta T}{t} = \frac{1}{2} \omega \varepsilon_0 \varepsilon''_{\rm eff} \int_V (\vec{E}^* \cdot \vec{E}) dV + \frac{1}{2} \omega \mu_0 \mu''_{\rm eff} \int_V (\vec{B}^* \cdot \vec{B})$$

$$\tag{1}$$

M is the mass,  $C_p$  is the specific heat capacity,  $\Delta T$  is the change in temperature, t is time,  $\omega$  is frequency,  $\varepsilon_0$  is the permittivity of free space,  $\varepsilon''_{\rm eff}$  is the lossy permittivity of the material,  $\mu_0$  is the permeability of free space,  $\mu''_{\rm eff}$  is the lossy permeability of the material, V is volume,  $\vec{E}^*$  is the complex conjugate of the electric field,  $\vec{E}$  is the electric field,  $\vec{B}^*$  is the complex conjugate of the magnetic field, and  $\vec{B}$  is the magnetic field.

The magnitude of coupling of the impinging MW photon on a reaction mixture will strongly depend on the electric dipoles of the reaction constituents. Applying the Beer–Lambert assumption in absorption spectroscopy leads to the simple conclusion that the MW energy is absorbed by the material with the largest  $\varepsilon''$  and scattered by the material with the largest  $\varepsilon'$  term in the system. <sup>27</sup>

 $P_{\rm abs}$  for the solvent decreases with increasing reaction temperature, while  $P_{\rm abs}$  for the precursor and NiNP will be time dependent as the precursor is consumed and the NiNP grows. As the MW cross section of the precursor is orders of magnitude lower than for the NiNP, the largest change in MW absorption will reflect the size-dependent evolution of the NiNP's complex dielectric. To account for the change in MW absorption, a scaling law can be derived by considering the work of Gor'kov and Eliashberg  $^{40,41}$  and of Marquardt and

Nimtz,  $^{42,43}$  on the size-dependent dynamic electric susceptibility ( $x_e$ ) of metallic NPs in a MW field. The early studies demonstrated that the value of  $\varepsilon^*$  can be described within a quasi-DC quantum model when the size difference between the photons and the NPs is 6–8 orders of magnitude. The complex dielectric can be written as the Gorkov–Eliashberg equation:

$$\varepsilon^* = 1 + \frac{m^* k_{\rm F} (2r)^2}{20\pi^2 a_{\rm B}} + \frac{139}{1200\pi^2 a_{\rm B}} \left( 2 + i \frac{\omega m^* k_{\rm F} (2r)^3}{6\hbar} \right)$$
(2)

where  $m^*$  is the effective electron mass,  $a_{\rm B}$  is the Bohr radius, r is the radius of the NP,  $\omega$  is the frequency of EM radiation,  $k_{\rm F}$  is the magnitude of the Fermi wave vector, and  $\hbar$  is Planck's constant. The temperature dependency of the dielectric constant can thus be written by coupling the Debye equation  $^{27-30,45}$  to the Gorkov–Eliashberg equation, such that  $\varepsilon^*(T)$  is expressible as

$$\varepsilon^*(T) \cong \varepsilon'_0 \left( 1 + \frac{e^{-2/\Delta T}}{e^{1/\Delta T} + e^{-1/\Delta T}} \right) + i\varepsilon''_0 \left( 1 + \frac{e^{-1/\Delta T}}{e^{1/\Delta T} + e^{-1/\Delta T}} \right) \tag{3}$$

A detailed derivation of eq 3 is provided in the Supporting Information. The model predicts that as the metal NP's size and reaction temperature increase, the power absorbed also increases, creating a positive feedback loop of continuously increasing power absorption.

Using eqs 1-3, the evolving dielectric environment that leads to MW heating can be evaluated in terms of the size and temperature. In Figure 1A, the theoretical  $P_{abs}$  is compared as a function of temperature for single molecules of oleylamine (OAm), Ni(acac)<sub>2</sub>, HAuCl<sub>4</sub>, and single 4 and 6 nm Ni and AuNPs. The 8 nm AuNP and monomers are also plotted in Figure 1A for comparison. Using eq 1, the theoretical  $P_{abs}$  is calculated from dielectric measurements at 2.45 GHz at room temperature on neat material using a vector network analyzer (VNA). Tan  $\delta$  for OAm is 0.040, for Ni(acac)<sub>2</sub> is 0.006, and for HAuCl<sub>4</sub> is 0.031 (though this number is complicated by the highly hygroscopic nature of HAuCl<sub>4</sub>), and the predicted values for 4 and 6 nm Ni and Au are derived using eq 2. From the tan  $\delta$  values, the order of  $P_{abs}$  will be Ni > OAm > Ni(acac)<sub>2</sub> for the neat materials. The same behavior is observed for the AuNPs. This leads to the conclusion that in the formation of NiNPs. during the reaction, the contribution of Ni(acac), to MW absorption is nominal, as at this concentration of Ni(acac)<sub>2</sub> (0.15 mmol) to OAm (45 mmol), the MW power absorbed by Ni(acac)<sub>2</sub> will be 4 orders of magnitude lower than by OAm. As Ni nucleates, it becomes the dominant absorbing species and is expected to increase the reaction temperature as the NiNP grows larger at fixed MW power. The same trend by analogy will be observed for AuNP growth within the MW field.

As shown in eqs 1–3, the cross section for MW absorption for the metal NP evolves in time as the NP grows, and the precursor is depleted. Therefore, as a reaction progresses to completion, MW absorption is expected to evolve from simple dipolar polarization-driven motion of precursor and solvent molecules to contributions arising from NP absorption and scattering, depending on the material's dielectric.

The predicted heating vs NiNP size correlation is graphed in Figure 1B, while the curve for AuNP is plotted in Figure 1C. The solid line represents the predicted reaction trajectory assuming normal diffusion controlled growth in both graphs. Inspection of Figure 1B confirms that at the temperature of the reaction (280 °C), absorption by the 20 nm NiNP is an order

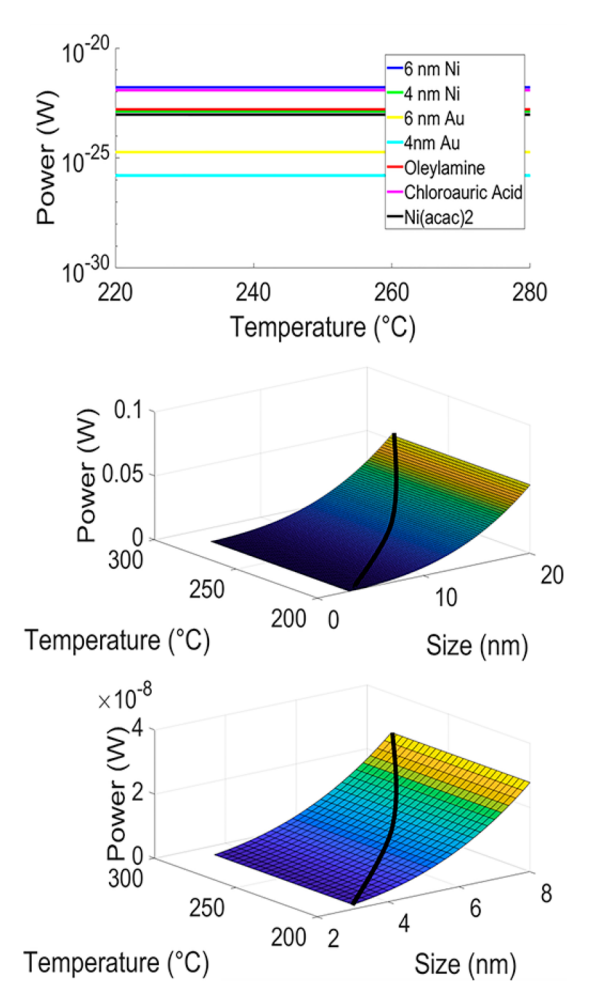


Figure 1. (A) Theoretical  $P_{\rm abs}$  vs temperature plot for oleylamine (OAm), Ni(acac)<sub>2</sub>, HAuCl<sub>4</sub>, 4 nm, and 6 nm NiNP and AuNP based on experimental room temperature dielectric measurements on neat materials. (B) Plot of  $P_{\rm abs}$  vs size and reaction temperature for NiNPs based on the size- and temperature-dependent change in permittivity (eqs 2 and 3). (C) Plot of  $P_{\rm abs}$  vs size and reaction temperature for AuNPs based on the size- and temperature-dependent change in permittivity (eqs 2 and 3). In (B) and (C) the solid line is a guide to eye for the reaction trajectory.

of magnitude larger than by the 3 nm NiNP. For the 8 nm AuNP, the heating curve is steeper than for Ni reflecting the increased  $\varepsilon''$  contribution to heating as Au increases in size (larger  $\varepsilon''$  or Au  $\nu s$  Ni). In addition, the AuNP reaction is held at 150 °C and is not allowed reach the boiling point of the solvent. Based on the theoretical heat plots in Figure 1B,C, the increased dielectric absorption leading to higher reaction temperatures as the metal NP grows may explain the MW enhanced rates and control observed in MW-based reactions.

**Evidence of Finke–Watzky Growth.** The growth of AuNPs under mild reducing conditions was originally described within the autocatalytic mechanism by Turkevich, and theoretically described by Finke and reported by others. The autocatalytic mechanism was extended to explain Ni growth under mildly reducing conditions in organic solvents by Tilley *et al.* In both cases the autocatalytic growth occurs for reactions performed below supersaturation conditions, wherein burst nucleation cannot occur due to the slow continuous formation of reactive M<sup>0</sup> monomers from M(II) ionic precursors. The autocatalytic mechanistic behavior for

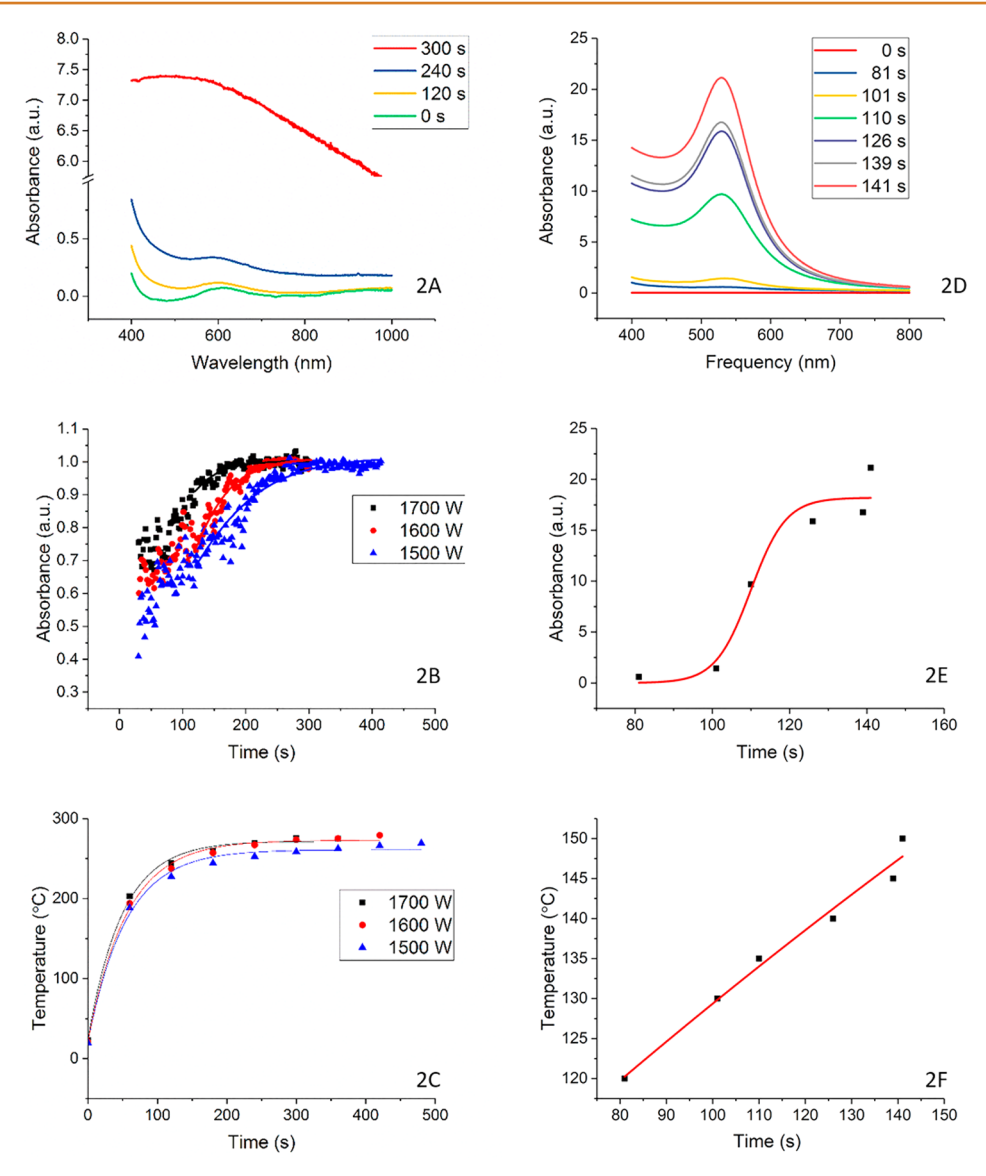


Figure 2. Time-dependent change in optical absorption of 0.01 M Ni(acac)<sub>2</sub> irradiated in OAm at 2.45 GHz. (A) Absorption spectrum at t=0, 120, 240, and 300 s for 1700 W irradiation. (B) A plot of  $A_{488}$  vs time at 1500, 1600, and 1700 W, with a sigmoidal fit. (C) A plot of time and temperature at 1500, 1600, and 1700 W. (A–C) Number of runs are n=3, though error bars are left out for clarity of the figure. Time-dependent change in optical absorption of 0.01 M HAuCl<sub>4</sub> irradiated in OAm at 2.45 GHz. (D) Absorption spectrum at t=0, 81, 101, 110, 126, 139, and 141 s, n=3. (E) A plot of  $A_{530}$  vs time at 150 W, with a sigmoidal fit, n=1. (F) A plot of time and temperature for AuNP synthesis, n=1.

the growth of metal NPs thus reflects the kinetic barrier for formation of M<sup>0</sup> monomers effectively suppressing nuclei formation. 33,34 The autocatalytic growth mechanism is described effectively as a two-step mechanism with nucleation in step 1,  $M_{\text{monomer}}^0 \rightarrow M_{\text{crit}}$  with a rate of  $k_1$  ( $M_{\text{crit}}$  is the critical nuclei), followed by the addition of additional monomer to generate a larger nuclei, where  $nM^0_{monomer} + M_{crit} \rightarrow M^*$  with a rate of  $k_2$ . The growth to the final NP size occurs by repeating step 2 so that M\* represents a continuously evolving larger nuclei. In effect, the final M NP size is achieved by continuous growth from the evolving nuclei once the monomer is depleted, such that  $nM^0_{\text{monomer}} + M^* \rightarrow M$  NP. It is worth noting that the autocatalytic mechanism equations are often misinterpreted as formation of two-nuclei due to the nomenclature being erroneously interpreted as new nuclei rather than increasing nuclei size. 17,33,35

In the autocatalytic mechanism the rate of nucleation  $(k_1)$  therefore is slow relative to the rate of growth  $(k_2)$  due to the surface energy. Since  $k_1 \ll k_2$ , growth from the initially formed nuclei is energetically favored over formation of new nuclei. The kinetic slow step is the amine reduction of the metal complex to produce  $M^0$  monomers prior to nucleation of a critical sized cluster.  $^{14,33}$ 

In the nomenclature of the autocatalytic mechanism the ratio of growth to nucleation rates, that is,  $k_2[\mathrm{M_{SA}}]/k_1$ , is defined as the  $R_{\mathrm{FW}}$  value, where  $\mathrm{M_{SA}}$  is the number of surface atoms on the growing nuclei. High  $R_{\mathrm{FW}}$  values indicate a high level of kinetic control, and at high R values, the reaction produces smaller NPs with a tighter size dispersity and *vice versa* for a low  $R_{\mathrm{FW}}$  value. A correlation between  $k_1$  and  $k_2$  can easily be derived from the rate expression expressed at constant temperature with respect to the growing M\* (M is Au or Ni).<sup>36</sup>

The rate of formation of d[M NP]/dt can thus be expressed as eq 4:

$$\frac{d}{dt}[MNP] = -k_1[M_{salt}] + k_2[M_{salt}][M^*]$$
 (4)

while the depletion of monomer  $(M^0_{monomer}/dt)$  can be expressed as

$$-\frac{d}{dt}[M^{0}] = k_{1}[M_{\text{salt}}] + k_{2}[M_{\text{salt}}][M^{*}]$$
(5)

In the reaction, it is assumed that the M\* concentration is invariant in time  $(d[M^*]/dt \sim 0)$  and will be equal to the concentration of critical nuclei formed at the nucleation. [M\*] during the reaction can be evaluated

$$[M^*]_t = \frac{[M_{\text{salt}}]_0 + [M_{\text{crit}}]_0}{1 + \frac{[M_{\text{salt}}]_0}{[M_{\text{crit}}]_0} e^{-([M_{\text{salt}}]_0 + [M_{\text{crit}}]_0)kt}}$$
(6)

where  $[M_{salt}]$  is the concentration of the precursor  $(Ni(acac)_2 \text{ or } HAuCl_4)$ , and  $[M_{crit}]_0$  is the critical concentration of nuclei to trigger NP growth. Solving eq 6 produces a sigmoidal growth curve at large R values.

By coupling the predictions of eqs 4 and 6 to the MW cross section for a growing metal NP (Figure 1), a large value of  $R_{\rm FW}$  should arise leading to a narrow dispersity. From the dielectric arguments, the growth rate will increase as the NP volume increases ( $V \propto r^3$ ) and herefore as  $P_{\rm abs}$ , which is proportional to the MW power and MW cross section, while the nucleation rate will remain constant at constant temperature or follow an Arrhenius behavior as the reaction temperature increases. It is worth noting that the influence of MW absorption of energy on the kinetic rates would theoretically continue to enhance the reaction behavior until either all the precursor in the initial solution is consumed or until a steady state is reached at which heat being emitted by the NPs back into the solution is equivalent to the heat being generated by the NP's power absorption.

To test this hypothesis, the growth mechanism for Ni and Au in a MW cavity is evaluated using absorption spectroscopy to follow the increase in the localized surface plasmon intensity for Ni and Au during MW irradiation. The Ni absorption was followed in real time, while the AuNP results were analyzed at selected time-points. The NiNP reaction is carried out at 1500, 1600, and 1700~W~(2.45~GHz) in a single pass cavity. The Au reactions were carried out at 150~W~in~a single mode cavity.

Inspection of the absorption properties of Ni(acac)<sub>2</sub> and NiNPs in solution reveals that Ni(acac)<sub>2</sub> does not absorb at 488 nm, while for the NiNP, a strong extinction feature attributable to the localized surface plasmon is observed at 488 nm (Figure 2A). The nonoverlapping absorption simplifies monitoring of Ni growth, allowing the rate of growth of Ni\* (d[Ni]/dt) to be directly monitored by plotting the change in the Ni absorption at 488 nm as a function of time, as absorption intensity will scale linearly with [Ni] following from the Beer–Lambert law.

In Figure 2A, growth of Ni was monitored by measuring the absorption spectrum with a UV-vis spectrometer at defined time points (0, 120 s, 240 s, and  $t_{\infty}$ , where  $t_{\infty}$  is the time point at which all precursor has converted into NiNPs). Each line is the average of three runs in the UV-vis. In Figure 2B growth was monitored at 488 nm ( $A_{488}$ ) during continuous irradiation with absorption data collected every 2.5 s from 0 to  $t_{\infty}$ . Each line is the average of three runs in the Gerling, smoothed with boxcar averaging (window of 3). The value of  $t_{\infty}$  varies from

300 to 450 s depending on the power applied. As can be seen in Figure 2C, the thermal ramp stabilizes beyond  $\sim$ 120 s. The temperature at each time point at a given power only varied 2–4 °C.

In an effort to baseline the studies to a well-known autocatalytic reaction, the same approach was applied to monitor AuNP growth in a MW cavity. In Figure 2D, the localized surface plasmon for a AuNP was followed in order to monitor the growth rate of 8 nm AuNP carried out at a maximum temperature of 150 °C at 150 W. The reaction was monitored at fixed time points (0, 81, 101, 110, 126, 139, and 141 s) during the growth, and the change in the absorption value is plotted in Figure 2E. The reaction asymptotes after 120 s at a temperature of 140 °C. Unlike the Ni reaction, a single power was carried out (150 W), and the maximum temperature was set at 150 °C, thus in Figure 2F, only the linear region for heating OAm is plotted.

To evaluate the correlation of the absorption changes for Ni and AuNPs with  $d[\mathrm{M}^*]/dt$ , it should be remembered the extinction coefficient  $(\varepsilon)$  will follow a simple size-dependent scaling function  $(\varepsilon \propto r^3)$  if the NPs remain spherical. The assumption of near sphericity is confirmed by the TEM data, wherein Ni spheres of ~25 nm (Figure 3) and Au spheres of 12 nm (Figure 4) are formed from thermal decomposition at 2.45 GHz. The size-dependent scaling for the absorption behavior for can thus be estimated by considering the Drude model, which predicts that the dielectric dispersion will scale with the number of metal atoms. For Au, the localized surface plasmon can be effectively followed to monitor the number of AuNPs in solution;  $^{37,38}$  however, for Ni which does not exhibit a well-defined plasmon modes, the Ni absorption manifold will show only intensity and not spectral changes.

By using the size-dependent extinction value for Ni, the experimental UV—vis data (Figures 2A, SI2, and SI3) can be fit to the autocatalytic expression (eq 4), yielding a  $k_1$  value of 2.43  $\times$  10<sup>-5</sup>  $\pm$  2.66  $\times$  10<sup>-5</sup> s<sup>-1</sup> and a  $k_2$  value of 1.20  $\times$  10<sup>-2</sup>  $\pm$  0.006 M·s<sup>-1</sup>. The reported values for Ni grown in the presence of trioctylphosphine at 0.06 M Ni(acac)<sub>2</sub> in OAm are  $k_1 = 1.5 \times 10^{-5}$  s<sup>-1</sup> and  $k_2 = 1.1 \times 10^{-2}$  M·s<sup>-1</sup>. The value of  $k_1$  is slightly enhanced, while  $k_2$  is unchanged, albeit the reaction conditions are different. The experimental UV—vis data for the AuNP (Figure 2E) fit to eq 4 yield values for  $k_1 = 1.21 \times 10^{-5} \pm 1.53 \times 10^{-6}$  s<sup>-1</sup> and  $k_2 = 0.102 \times 10^{-2} \pm 1.53 \times 10^{-4}$  M·s<sup>-1</sup>. While no values were reported for AuNPs for  $k_1$  and  $k_2$ , extraction of the values from Liu's results yields rates of  $k_1 \sim 1 \times 10^{-8}$  s<sup>-1</sup> and  $k_2 \sim 1 \times 10^{-4}$  M·s<sup>-1</sup>. The enhancement in  $k_1$  is notable but requires further investigation to conclusively correlate the rate to the MW effects.

As expected for an autocatalytic reaction,  $k_1$  ( $10^{-5}$  s<sup>-1</sup>)  $\ll k_2$  ( $10^{-2}$  M·s<sup>-1</sup>) for the observed metal NP growth. The agreement in the measured and reported kinetic rates for metal NP growth in a convective reaction and in a MW supports the conclusion that reactions follow the same thermodynamic paths and the observed MW effects arises from the efficiency of coupling MW energy to the reaction components to reach reaction temperature, rather than invoking special MW processes, as suggested in earlier literature.

 $R_{\text{FW}}$  Values. A notable effect in the MW is the power dependence of the size dispersion of the Ni (Figure 3). The power-dependent Ni sizes at the completion of the reaction are 27.5  $\pm$  9.12 nm at 1500 W, 26.7  $\pm$  5.84 nm at 1600 W, and 21.4  $\pm$  2.33 nm at 1700 W. The TEM distributions observed

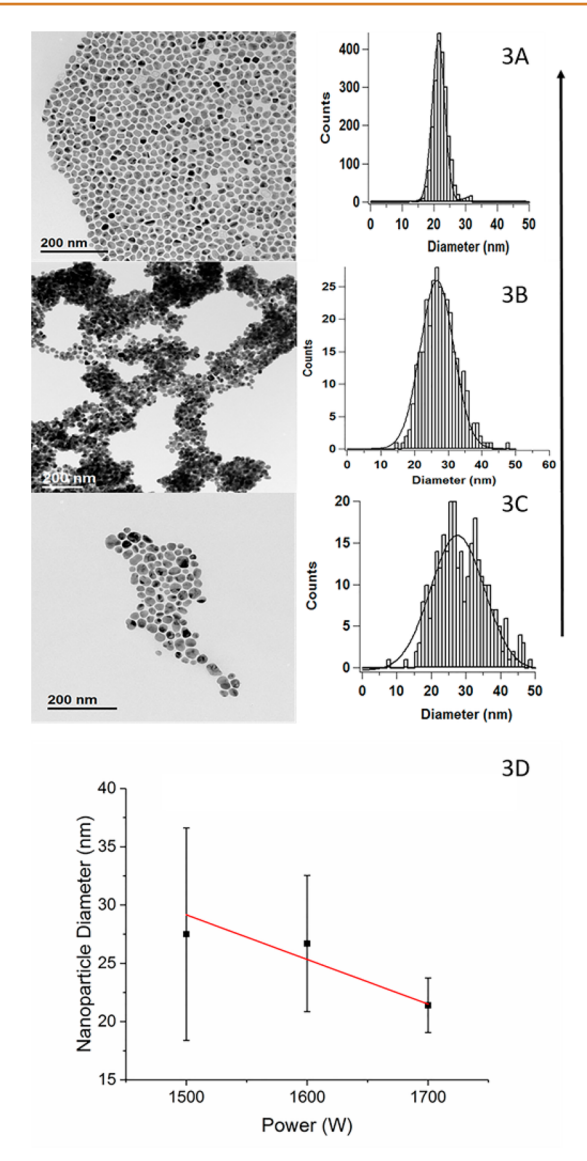


Figure 3. TEM of Ni NPs formed at (A) 1700, (B) 1600, and (C) 1500 W with distribution curves of >300 NPs. (D) A plot of the average NP diameter formed at each power, with error bars of the fwhm showing that the higher the power, the smaller the NP size and the tighter the distribution.

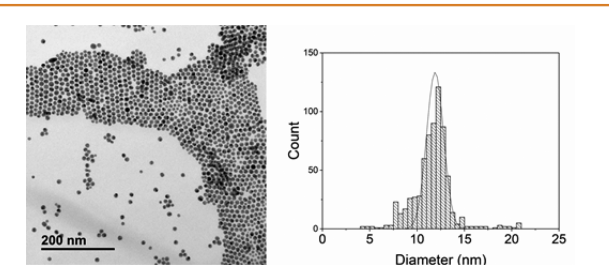


Figure 4. TEM of Au NPs formed at 150 W with distribution curves of >300 NPs.

for the power-dependent Ni reactions do not show the typical tailing to smaller sizes observed in Ostwald ripening and exhibit a size distribution much narrower than observed for isolated NiNPs grown *via* hot-injection synthetic methods. 1,7,41,42

The power-dependent enhancement in dispersity for NPs grown in a MW is readily explained within the F-W

autocatalytic mechanism without invoking MW special effects. In a MW, higher power will not affect the rates but rather the number of nuclei produced at the initiation of the reaction. In addition, within a MW cavity nucleation will be uniform since heating is volumetric and does not possess thermal gradients typical of convections reactions. Thus, the larger  $R_{\rm FW}$  values will lead to better-controlled growth and tighter size distributions.

The assumption that the power-dependent narrowing of size dispersity is related to MW absorption can be demonstrated by calculating the power-dependent  $R_{\rm FW}$  value. F-W assumed the value of  $R_{\rm FW}$  can be approximated from the number of NPs in solution at the end of the reaction, since the number of nuclei is invariant during the reaction allowing  $R_{\rm FW} \sim k_2 [\rm M_{NP}]/k_1$ . A more rigorous calculation would require the number of surface atoms (M<sub>SA</sub>) to be explicitly known as the NP grows, which is experimentally intractable.

Using the formalism of F-W, for the growth of metal NPs, it is assumed the number of nuclei at the start of the reaction  $(M^*)$  are equal to the number of NPs at the completion of the reaction  $(M_{NP})$ . The nuclei concentration can therefore be calculated from the solution absorption spectrum using the size-dependent Mie scattering absorption cross-section of a single NP. The calculation of the number of nuclei follows from the methods employed in CdSe QDs and AuNPs. A more through derivation is in the Supporting Information. It is worth noting the F-W reactions are carried out below saturation (LaMer limit), making the estimation of nuclei easier. For the NiNP power-dependent study, the calculation yields concentrations of  $3.42 \times 10^{-6}$  M (1500 W),  $4.56 \times 10^{-6}$  M (1600 W), and  $1.47 \times 10^{-5}$  M (1700 W).

The validity of the assumption from F-W that the number of nuclei in the reaction is equivalent to the final NP concentration can be tested by analyzing the number of nuclei at the initiation of the reaction. TEM images of NiNPs 2 min into the reaction (1500W) are 3 nm in size (Figure SI5) and as shown in Figure 3 reach 27.6 nm. Using the Mie scattering extinction value for a 3 nm Ni yields a value of  $3.2 \times 10^{-5}$  M for the number of NPs in solution. The value is within experimental agreement with the number of NPs at the completion of the reaction. Such agreement supports the F-W assumption, as this would not be expected in a classical LaMer model where small NPs dissolve to form larger NPs.  $^{3.5}$ 

From the calculated  $k_1$ ,  $k_2$ , and number of NPs, the power-dependent  $R_{\rm FW}$  values for the Ni reactions are  $1.77 \times 10^{-3}$  (1500 W),  $2.36 \times 10^{-3}$  (1600 W), and  $7.07 \times 10^{-3}$  (1700 W). Similarly, the AuNPs grown at 150 W have a concentration of  $1.36 \times 10^{-4}$  M and yield an  $R_{\rm FW}$  value of  $9.25 \times 10^{-3}$ . The narrowing of size dispersity observed for the NiNPs with increasing power correlates with the change in NP concentration and thus the  $R_{\rm FW}$  values. In effect, increased power increases the number of nuclei in the reaction due to the more efficient absorption of energy within a MW cavity where volumetric heating occurs.

Role of Magnetic Moment (Permeability) And Surface Oxides on MW Heating. From the above results it is clear the growth of Ni and Au in a MW follows the expected autocatalytic growth behavior. The improvement of metal NP formation in the MW, as reflected by the dispersity with increasing power, reflects the more efficient conversion of MW energy leading to more uniform nuclei formation with a power-dependent  $R_{\rm FW}$  value and not changes to the reaction mechanism. For complete understanding of the special effects

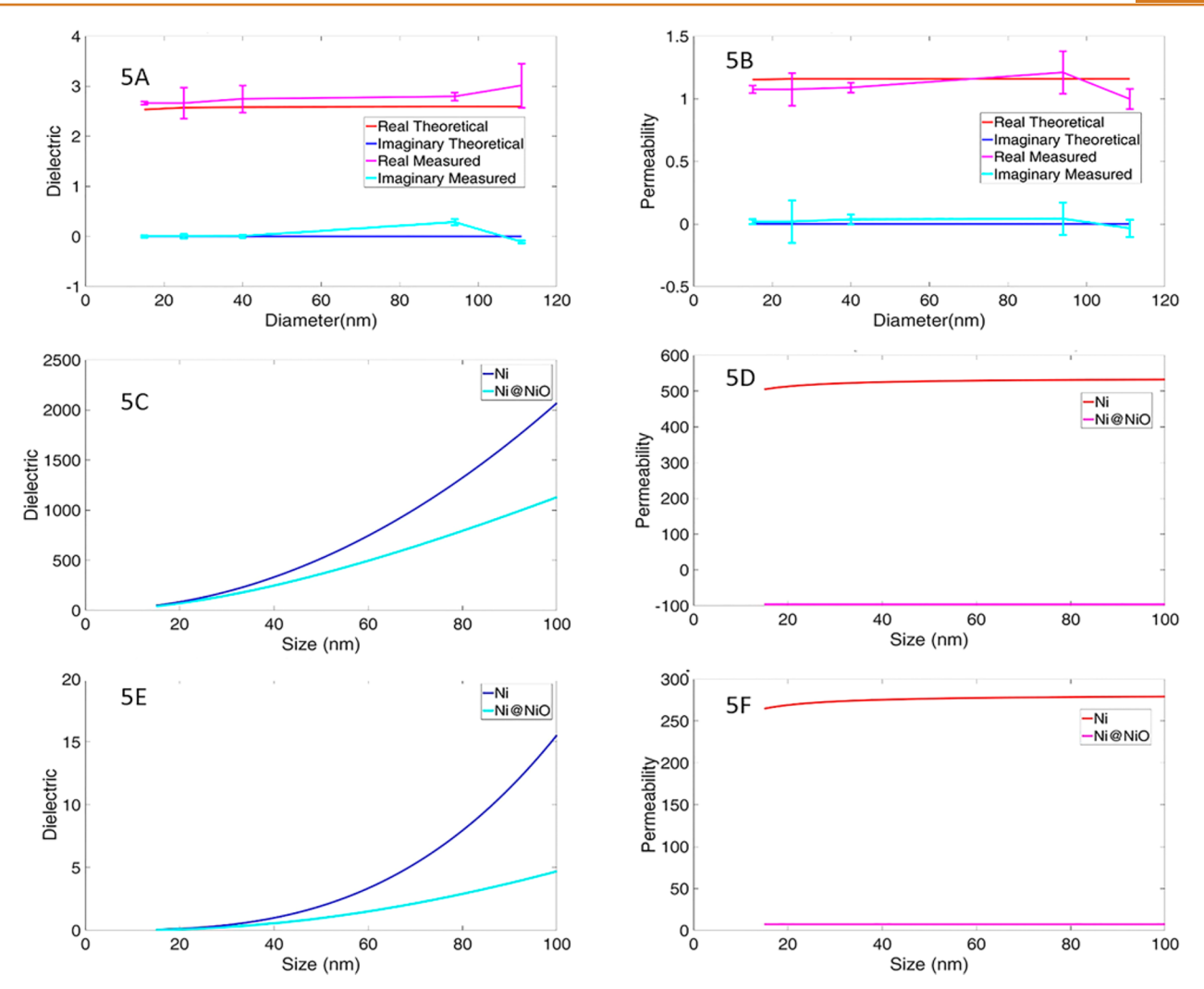


Figure 5. (A) and (B) Complex permittivity and permeability of Ni@NiO NPs embedded in wax theoretically compared to the measured; n = 3. (C-F) Theoretical complex permittivity and permeability of Ni vs Ni@NiO NPs, showing that the NiO layer suppresses the dielectric and the permeability.

that might arise for MW grown materials, the size dependence of permeability and the presence of a surface oxide forming a core@shell motif should be considered theoretically.

In analogy to the effect of size-dependent permittivity on MW reactions (eqs 1–3), the size-dependent complex permeability ( $\mu^*$ ) can be calculated, although in this study the contribution will be small in the temperature-dependent growth as the magnetic field strength is 1/377 the electric field strength, <sup>46</sup> and the reaction temperatures are well above the blocking temperature for the NiNPs (15 nm super paramagnet limit) in this study. <sup>47,48</sup>

The frequency- and size-dependent permeability can be described by the Landau–Lifshitz–Gilbert expression: <sup>49,50</sup>

$$\mu^* = 1 + \frac{(4\pi M_s)^2}{2K - \left(\frac{\omega}{2\pi\gamma}\right)^2 + i\alpha(4\pi M_s)\left(\frac{\omega}{2\pi\gamma}\right)}$$
(7)

where  $\gamma$  is the gyromagnetic ratio,  $\alpha$  is the dampening factor, K is the crystalline anisotropy, and  $M_{\rm s}$  is the saturation magnetization. Both K and  $M_{\rm s}$  are size and shape dependent, with the size dependency of K written as  $^{51}$ 

$$K = K_{\rm v} + \frac{6}{x}K_{\rm s} \tag{8}$$

in which  $K_{\rm v}$  is the crystalline anisotropy,  $K_{\rm s}$  is the surface anisotropy, and x is the diameter of the NP. The size dependency of  $M_{\rm s}$  is  $^{52}$ 

$$M_{\text{s(nano)}} \approx M_{\text{s(bulk)}} \left( 1 - \frac{2d}{x} \left( 1 + \frac{S_{\text{vib}}}{3R} \right) \right)$$
 (9)

where  $M_{\rm s(bulk)}$  is the bulk magnetic saturation moment, d is average distance between atomic centers, x is the diameter of the NP,  $S_{\rm vib}$  is the vibrational melting entropy, and R is the ideal gas constant.

The presence of an oxide forming a core@shell structure will have an impact on the permeability and the permittivity. In the case of a core@shell NP, the change to the permeability effects is proportional to the value of  $M_{\rm s(nano)}$ . When the shell is antiferromagnetic (AFM), as is the case of NiO, the saturation moment for the core can be redefined as a core@shell moment  $(M'_{\rm s(nano)})$ 

$$M'_{s(nano)} = \frac{2K}{4\pi H_{ex}} + \frac{J}{x_c H_{ex}}$$
 (10)

where  $H_{\rm ex}$  is the exchange bias coercivity, J is the exchange bias constant, K is the core anisotropy, and  $x_c$  is the diameter of the core. The effect on the MW reaction for Ni and Au is insignificant, reflecting the reaction temperature, NP size, and magnetic moment of the metal cores.

The effect on permittivity will be more significant though, as an oxide has a much lower dielectric value and thus a lower  $P_{\rm abs}$ . The effect of a surface oxide is easily seen by considering the size-dependent permittivity for Ni by derivation of the size-dependent complex dielectric ( $\varepsilon^*$ ) in eq 2. The effective  $\varepsilon^*$  value for a Ni@NiO core@shell NP can be calculated using the Maxwell Garnett effective medium theory, which determines the effective polarizability ( $\alpha_k$ ), and the Claussius—Mossoti equation, which relates  $\alpha_k$  to  $\varepsilon^*_{\rm eff}$ , such that

$$\varepsilon^*_{\text{eff}} = 1 + \frac{\alpha_k}{1 - \alpha_k/3} \tag{11}$$

and

$$\alpha_{k} = 3 \frac{(\varepsilon^{*}_{s} - 1)(\varepsilon^{*}_{c} + 2\varepsilon^{*}_{s}) + g(2\varepsilon^{*}_{s} + 1)(\varepsilon^{*}_{c} - \varepsilon^{*}_{s})}{(\varepsilon^{*}_{s} + 2)(\varepsilon^{*}_{c} + 2\varepsilon^{*}_{s}) + 2g(\varepsilon^{*}_{s} - 1)(\varepsilon^{*}_{c} - \varepsilon^{*}_{s})}$$

$$(12)$$

where  $\varepsilon_s^*$  is the dielectric of the shell,  $\varepsilon_c^*$  is the dielectric of the core, and g is the radius of the core squared divided by the radius of the NP squared.

From eqs 11 and 12, the impact of a native 1.2 nm oxide on a 20 nm NiNP vs a pure NiNP results in an order of magnitude higher  $P_{\rm abs}$  for Ni vs Ni@NiO (Figure SI6). Based on the theoretical predictions, the presence of NiO formed during the reaction would effectively slow the heating rate. The effect of oxides on AuNPs is assumed to be minor due to surface passivation, and thus while the equations can be applied to AuNP, it is not considered further in this manuscript to conserve space.

The size-dependent behavior for isolated NiNPs embedded in wax can be used to test the predictions in eqs 7-12 (Figure 5A-B). As one can see, the wax and NiO layers flatten the difference between sizes, but there is a slight rise with size in the dielectric and, from 15 to 25 nm, in the permeability. Figure 5C-F also shows data with respect to the theoretical permittivity and permeability of NiNPs from 15 to 111 nm with and without an oxide layer without the wax matrix, showing the NiO layer suppresses the permeability and permittivity. For the dielectric, both the real and the imaginary components rise sharply with size, whereas for the permeability, the real and imaginary components reach a maximum just above the single domain size (~20 nm). The NiNPs, as analyzed in the VNA, show that the oxidation layer makes a pronounced difference to the final measured results, once the oxide layer is accounted for, theory and experiment match.

For a MW reaction, the measurements allow speculation of the impact on a reaction for NiNP growth if an oxide layer is present during the growth step. From TEM images (Figure SI7), the thickness of the oxide is 1.2 nm, consistent with the reported values. The 1.2 nm oxide layer would lead to a large suppression in  $\varepsilon^*$  and  $\mu^*$  accompanied by an order of magnitude suppression of  $P_{\rm abs.}$  While it would be exciting to measure the MW dielectric spectrum of the NiNPs during growth, the experiment is impractical as in situ MW absorption experiments are difficult due to the difference of 5–6 orders of magnitude between the power needed to induce a MW-assisted chemical reaction (kW) and the power needed to measure

small dielectric perturbations (mW) caused by a sample in a field.

#### **CONCLUSIONS**

Microwave chemistry has come a long way since the midtwentieth century. Given its potential for green chemistry applications and rapid prototyping of novel materials, a deeper understanding of the exact nature of the evolution of a chemical reaction is desirable. By combining theoretical work with static and dynamic measurements of metal NP synthesis, the enhanced dipersity and growth behavior of metal NPs in a MW cavity can be understood purely from mechanistic arguments and thermodynamics.

The theoretical work shows that metal NPs will grow until all of the precursor is consumed, and their final size will then be dependent on the initial concentration of the solution and the nucleation process. Classical nucleation theory says that the nucleation step is instantaneous, then growth occurs on the nuclei to form NPs. This agrees with the data from the laser absorption and UV—vis experiments, which show the conversion of the precursor into NPs at rates that correspond with the increase in power, with lower powers having slower formation times. The laser absorption data also confirm that NPs made in a MW-assisted reaction follow F-W theory, with a sigmoidal dependence of the growth of NPs from solution. The UV—vis data allow us to extract  $k_1$  and  $k_2$  values from the reactions, giving us more insight into the kinetics of the reaction.

The observation that the enhanced reaction rate for a metal grown in a MW cavity arises from increased MW interactions with the growing NP may actually provide the thermodynamic basis for the observed improvement in metal NP formation within a MW reported in Au and Fe/Pt $^{10,53}$  and supports the findings of Liu *et al.*<sup>54</sup> for growth of silver NPs in a MW cavity. Thus, the dielectric arguments leading to MW enhanced reaction rates can be tied to the autocatalytic process by measuring the rate of reaction as a function of power.

# **EXPERIMENTAL SECTION**

**Materials.** The NiNP standards and 15, 25, and 40 nm *fcc*-NiNPs were prepared and characterized previously (Figure SI7),<sup>41</sup> and the 94 and 111 nm NiNPs were synthesized as described below. Nickel acetylacetonate (Ni(acac)<sub>2</sub>), 70% oleylamine (OAm), and 90% oleic acid (OA) were purchased from Sigma–Aldrich. Paraffin wax and solvents were used without further purification.

Synthesis of Ni Standards (94 and 111 nm). Spherical fcc-NiNPs 94 and 111 nm in diameter were synthetically prepared using MW-assisted decomposition of Ni(acac)<sub>2</sub> in a 5:1 OAm-to-OA mole ratio medium. The synthetic preparation of the spherical, 94- (111) nm fcc-Ni was carried out by mixing 3 mmol (6 mmol) of Ni(acac)<sub>2</sub>, 50 mmol of OAm, and 10 mmol of OA in a round-bottom flask and degassing under vacuum at 110 °C. Nine mL of the clear, deep blue solution was transferred under ambient conditions into a G30 (30 mL) Anton Paar MW vessel and capped. No stir bar or inert atmosphere was used in the reaction vessel. The vessel was placed into the Anton Paar Monowave 300-MW system, and the reaction temperature was ramped up to 280 °C at 300 W power, held at 280 °C for 8 min, and cooled by forced air to 55 °C. NPs were isolated from the reaction mixture by magnetic separation from the solution, sonication in 10 mL toluene to resuspend the Ni, and a second magnetic separation. The resultant solid was dispersed in 10 mL methanol with sonication and magnetically separated. The washing procedure was repeated two more times, then the NPs were dried at room temperature under vacuum.

**Synthesis of AuNPs.** The AuNPs were formed by creating a 0.01 M solution of chloroauric acid in 36.8 mL of OAm. This solution was heated to 60  $^{\circ}\text{C}$  and degassed under vacuum. For each reaction, 4 mL of the precursor solution was added to a microwave vial with a stir bar. The vials were then placed into a CEM microwave using a frequency of 2.45 GHz at constant power of 150 W to reach varying temperatures ranging between 120 and 150  $^{\circ}\text{C}$ . When the microwave reached temperature, the temperature was held for 1 s, then immediately air cooled to 55  $^{\circ}\text{C}$ .

Characterization. The 94 and 111 nm NiNPs (Figure SI8) and the AuNPs were fully characterized by pXRD and TEM. The 94 and 111 nm NiNPs can be indexed to the fcc structure (card PDF # 01-08-7128) measured on a Rigaku DMAX 300 Ultima III Powder X-ray diffractometer (using Cu  $K_{\alpha}$   $\lambda$  = 1.5418 Å radiation). The AuNPs can be indexed to the fcc structure (card PDF # 98-000-0056) measured on a Rigaku DMAX 300 Ultima III Powder X-ray diffractometer (using Cu  $K_{\alpha}$   $\lambda = 1.5418$  Å radiation). The size, size dispersity, and morphology were measured by transmission electron microscopy (TEM) with a JEM-ARM200cF electron microscope at 200 kV accelerating voltage. Diluted NP samples were drop-cast from dispersion in toluene onto 300-mesh copper grids and left to dry under reduced pressure overnight. Histograms generated from image capture of >300 nanocrystals in ImageJ were used to generate the size distribution curves. Solution absorption spectra were obtained using a Varian Cary 50 UV-vis spectrophotometer in a 1 cm quartz cuvette.

Complex Dielectric Measurements. Complex dielectric measurements at 2.45 GHz (298 K) were performed on isolated NiNPs (15, 25, 40, 94, and 111 nm) using a vector network analyzer (Anritsu Lightning E model 37347E) impedance matched to a coaxial cavity manufactured by Damaskos, Inc. (M07T). The measurements were performed on isolated Ni@NiO NPs (15, 25, 40, 94, and 111 nm) blended in a 5% v/v ratio with paraffin wax and molded into a toroidal shape that fit into the coaxial cavity made by Damaskos, Inc. The Nicholson–Ross–Weir algorithm in the Damaskos software was used to calculate the complex permittivity and permeability of the composites at 2.45 GHz.

To calculate the permittivity and permeability, effective medium theory (EMT) is employed for this calculation. The Maxwell Garnett theorem is ideal for a metallic inclusion in an insulator <sup>55,56</sup> and is thus the EMT is used for this calculation as well.

**Growth Kinetics.** The formation rate of NiNPs was monitored under MW irradiation at 2.45 GHz at 1500, 1600, and 1700 W using single-wavelength absorption spectroscopy at 488 nm (Ar<sup>+</sup> ion laser). The change in absorption intensity at 488 nm was monitored on a Si diode (ThorLabs DET10A) connected to an oscilloscope (LeCroy WaveRunner 6051) with data points recorded every 2.5 s for 450 s. The measurements were performed on a 0.01 M solution of Ni(acac)<sub>2</sub> in OAm. MW measurements were performed in a resonant cavity (TE<sub>013</sub>) coupled to a Gerling MW source with 10 mL of reaction solution contained in a square (1.4 cm  $\times$  1.4 cm) quartz reactor vessel. Figure SI1 shows the setup. Temperature and power were monitored actively during the reaction. The *in situ* measurement was validated by UV—vis measurements from 400 to 1000 nm at defined time intervals (120 s, 240 s, and final reaction time dependent on power used).

The AuNP reaction dynamics were measured at 2.45 GHz at 150 W in a single mode cavity (CEM). The change in plasmon absorption at 530 nm was monitored by UV—vis absorption at static time points (0, 81, 101, 110, 126, 139, and 141 s) using separate MW reaction vessels. To measure the absorption changes, a 0.1 mL aliquot was diluted in toluene. For sizing, TEM images were measured on the AuNPs isolated from the reaction mixture using about 5 mL of toluene and 1 mL of methanol. This process was repeated four times with sonication occurring after each toluene addition.

### **ASSOCIATED CONTENT**

# **S** Supporting Information

The Supporting Information is available free of charge on the ACS Publications website at DOI: 10.1021/acsnano.7b04040.

Detailed derivations of equations used in the theoretical calculations, figures of setup and additional supporting images for the characterization of the Ni samples are provided (PDF)

#### **AUTHOR INFORMATION**

### **Corresponding Author**

\*E-mail: strouse@chem.fsu.edu.

**ORCID** ®

Joseph B. Tracy: 0000-0002-3358-3703 Geoffrey F. Strouse: 0000-0003-0841-282X

#### **Author Contributions**

B.A. measured the power-dependent MW reactions, carried out the dielectric measurements and theoretical derivations, and assisted in the writing of the manuscript. C.D. carried out the AuNP reactions, while P.V. and B.L. prepared the Ni standards. P.V. and C.D. characterized the NPs. J.O. and J.T. assisted in the experimental design and interpretation. G.F.S. designed the project, assisted in interpretation, and conclusions and in the writing of the manuscript. All authors revised the manuscript.

#### Notes

The authors declare no competing financial interest.

### **ACKNOWLEDGMENTS**

G.F.S., B.A., and P.V. wish to thank the National Science Foundation CHE-1608364: SusChEM: Understanding Microwave Interactions to Control Magnetic Nanocrystal Growth from a Single Source Precursor. This project was supported (B.A., J.O.) in part by an appointment to the Research Participation Program at the Air Force Civil Engineer Center administered by the Oak Ridge Institute for Science and Education. B.B.L. and J.B.T. acknowledge a NSF grant CBET-1605699. The TEM imaging at FSU is supported by the Florida State University Research Foundation and through the National High Magnetic Field Laboratory National Science Foundation Cooperative Agreement DMR-1157490, the State of Florida, and Florida State University. TEM imaging at NC State was performed at the Analytical Instrumentation Facility (AIF), which is supported by the State of North Carolina and the National Science Foundation (award number ECCS-1542015). The AIF is a member of the North Carolina Research Triangle Nanotechnology Network (RTNN), a site in the National Nanotechnology Coordinated Infrastructure (NNCI).

# **REFERENCES**

- (1) Mourdikoudis, S.; Liz-Marzán, L. M. Oleylamine in Nanoparticle Synthesis. *Chem. Mater.* **2013**, *25*, 1465–1476.
- (2) Watzky, M. A.; Finke, R. G. Transition Metal Nanocluster Formation Kinetic and Mechanistic Studies. A New Mechanism when Hydrogen is the Reductant: Slow, Continuous Nucleation and Fast Autocatalytic Surface Growth. *J. Am. Chem. Soc.* **1997**, *119*, 10382–10400.
- (3) Jhung, S. H.; Jin, T.; Hwang, Y. K.; Chang, J. S. Microwave Effect in the Fast Synthesis of Microporous Materials: Which Stage Between Nucleation and Crystal Growth is Accelerated by Microwave Irradiation? *Chem. Eur. J.* **2007**, *13*, 4410–4417.
- (4) Gawande, M. B.; Shelke, S. N.; Zboril, R.; Varma, R. S. Microwave-Assisted Chemistry: Synthetic Applications for Rapid Assembly of Nanomaterials and Organics. *Acc. Chem. Res.* **2014**, *47*, 1338–1348.

(5) Washington, A. L.; Strouse, G. F. Microwave Synthesis of CdSe and CdTe Nanocrystals in Nonabsorbing Alkanes. *J. Am. Chem. Soc.* **2008**, *130*, 8916–8922.

- (6) Zedan, A. F.; Sappal, S.; Moussa, S.; El-Shall, M. S. Ligand-Controlled Microwave Synthesis of Cubic and Hexagonal CdSe Nanocrystals Supported on Graphene. Photoluminescence Quenching by Graphene. *J. Phys. Chem. C* **2010**, *114*, 19920–19927.
- (7) Gerbec, J. A.; Magana, D.; Washington, A.; Strouse, G. F. Microwave-Enhanced Reaction Rates for Nanoparticle Synthesis. *J. Am. Chem. Soc.* **2005**, *127*, 15791–15800.
- (8) Siramdas, R.; McLaurin, E. J. InP Nanocrystals with Color-Tunable Luminescence by Microwave-Assisted Ionic-Liquid Etching. *Chem. Mater.* **2017**, *29*, 2101–2109.
- (9) Muthuswamy, E.; Iskandar, A. S.; Amador, M. M.; Kauzlarich, S. M. Facile Synthesis of Germanium Nanoparticles with Size Control: Microwave Versus Conventional Heating. *Chem. Mater.* **2013**, 25, 1416–1422.
- (10) Carnevale, D. J.; Shatruk, M.; Strouse, G. F. Ligand Passivated Core—Shell FePt@ Co Nanomagnets Exhibiting Enhanced Energy Product. *Chem. Mater.* **2016**, 28, 5480–5487.
- (11) Bilecka, I.; Niederberger, M. Microwave Chemistry for Inorganic Nanomaterials Synthesis. *Nanoscale* **2010**, *2*, 1358–1374.
- (12) de la Hoz, A.; Diaz-Ortiz, A.; Moreno, A. Microwaves in Organic Synthesis. Thermal and Non-thermal Microwave Effects. *Chem. Soc. Rev.* **2005**, *34*, 164–178.
- (13) LaGrow, A. P.; Ingham, B.; Toney, M. F.; Tilley, R. D. Effect of Surfactant Concentration and Aggregation on the Growth Kinetics of Nickel Nanoparticles. *J. Phys. Chem. C* **2013**, *117*, 16709–16718.
- (14) Finney, E. E.; Finke, R. G. Nanocluster Nucleation and Growth Kinetic and Mechanistic Studies: A Review Emphasizing Transition-Metal Nanoclusters. J. Colloid Interface Sci. 2008, 317, 351–374.
- (15) Turkevich, J.; Stevenson, P. C.; Hillier, J. A Study of the Nucleation and Growth Processes in the Synthesis of Colloidal Gold. *Discuss. Faraday Soc.* **1951**, *11*, 55–75.
- (16) Polte, J. r.; Ahner, T. T.; Delissen, F.; Sokolov, S.; Emmerling, F.; Thünemann, A. F.; Kraehnert, R. Mechanism of Gold Nanoparticle Formation in the Classical Citrate Synthesis Method Derived from Coupled *In Situ* XANES and SAXS Evaluation. *J. Am. Chem. Soc.* **2010**, 132, 1296–1301.
- (17) Perala, S. R. K.; Kumar, S. On the Two-Step Mechanism for Synthesis of Transition-Metal Nanoparticles. *Langmuir* **2014**, *30*, 12703–12711.
- (18) Besson, C.; Finney, E. E.; Finke, R. G. A Mechanism for Transition-Metal Nanoparticle Self-Assembly. *J. Am. Chem. Soc.* **2005**, 127, 8179–8184.
- (19) Mondloch, J. E.; Yan, X.; Finke, R. G. Monitoring Supported-Nanocluster Heterogeneous Catalyst Formation: Product and Kinetic Evidence for a 2-Step, Nucleation and Autocatalytic Growth Mechanism of Pt (0) n Formation from H2PtCl6 on Al2O3 or TiO2. J. Am. Chem. Soc. 2009, 131, 6389–6396.
- (20) Bentea, L.; Watzky, M. A.; Finke, R. G. Sigmoidal Nucleation and Growth Curves Across Nature Fit by the Finke—Watzky Model of Slow Continuous Nucleation and Autocatalytic Growth: Explicit Formulas for the Lag and Growth Times Plus Other Key Insights. *J. Phys. Chem. C* 2017, 121, 5302—5312.
- (21) Kimling, J.; Maier, M.; Okenve, B.; Kotaidis, V.; Ballot, H.; Plech, A. Turkevich Method for Gold Nanoparticle Synthesis Revisited. *J. Phys. Chem. B* **2006**, *110*, 15700–15707.
- (22) Chen, Y.; Peng, D.-L.; Lin, D.; Luo, X. Preparation and Magnetic Properties of Nickel Nanoparticles *via* the Thermal Decomposition of Nickel Organometallic Precursor in Alkylamines. *Nanotechnology* **2007**, *18*, 505703.
- (23) Lu, G.; Li, X.; Jiang, H. Electrical and Shielding Properties of ABS Resin Filled with Nickel-Coated Carbon Fibers. *Compos. Sci. Technol.* **1996**, *56*, 193–200.
- (24) Rodríguez, A. M.; Prieto, P.; de la Hoz, A.; Díaz-Ortiz, A.; García, J. I. The Issue of 'Molecular Radiators' in Microwave-Assisted Reactions. Computational Calculations on Ring Closing Metathesis (RCM). Org. Biomol. Chem. 2014, 12, 2436–2445.

- (25) Rodríguez, A. M.; Prieto, P.; de la Hoz, A.; Díaz-Ortiz, Á.; Martín, D. R.; García, J. I. Influence of Polarity and Activation Energy in Microwave—Assisted Organic Synthesis (MAOS). *ChemistryOpen* **2015**, *4*, 308–317.
- (26) Chung, D. Electromagnetic Interference Shielding Effectiveness of Carbon Materials. *Carbon* **2001**, *39*, 279–285.
- (27) Metaxas, A. C.; Meredith, R. J. *Industrial Microwave Heating*; Institute of Engineering and Technology: London, United Kingdom, 1983.
- (28) Nix, F. C.; Shockley, W. Order-Disorder Transformations in Alloys. Rev. Mod. Phys. 1938, 10, 1.
- (29) Fröhlich, H. Theory of Dielectrics: Dielectric Constant and Dielectric Loss. Clarendon Press: Oxford, UK, 1958.
- (30) Jonscher, A. K. Dielectric Relaxation in Solids. J. Phys. D: Appl. Phys. 1999, 32, R57.
- (31) Henglein, A. Physicochemical Properties of Small Metal Particles in Solution: Microelectrode Reactions, Chemisorption, Composite Metal Particles, and the Atom-to-Metal Transition. *J. Phys. Chem.* **1993**, *97*, 5457–5471.
- (32) Zhang, Z.; Patel, R. C.; Kothari, R.; Johnson, C. P.; Friberg, S. E.; Aikens, P. A. Stable Silver Clusters and Nanoparticles Prepared in Polyacrylate and Inverse Micellar Solutions. *J. Phys. Chem. B* **2000**, *104*, 1176–1182.
- (33) Irzhak, V. The Mechanisms of the Formation of Metal-Containing Nanoparticles. *Ref. J. Chem.* **2016**, *6*, 370–404.
- (34) Watzky, M. A.; Finney, E. E.; Finke, R. G. Transition-Metal Nanocluster Size vs Formation Time and the Catalytically Effective Nucleus Number: A Mechanism-Based Treatment. J. Am. Chem. Soc. 2008, 130, 11959–11969.
- (35) Thanh, N. T.; Maclean, N.; Mahiddine, S. Mechanisms of Nucleation and Growth of Nanoparticles in Solution. *Chem. Rev.* **2014**, *114*, 7610–7630.
- (36) Mata-Perez, F.; Perez-Benito, J. F. The Kinetic Rate Law for Autocatalytic Reactions. J. Chem. Educ. 1987, 64 (11), 925.
- (37) Breshike, C. J.; Riskowski, R. A.; Strouse, G. F. Leaving Förster Resonance Energy Transfer Behind: Nanometal Surface Energy Transfer Predicts the Size-Enhanced Energy Coupling Between a Metal Nanoparticle and an Emitting Dipole. *J. Phys. Chem. C* **2013**, 117, 23942–23949.
- (38) Eustis, S.; El-Sayed, M. A. Why Gold Nanoparticles are More Precious than Pretty Gold: Noble Metal Surface Plasmon Resonance and its Enhancement of the Radiative and Nonradiative Properties of Nanocrystals of Different Shapes. *Chem. Soc. Rev.* **2006**, 35, 209–217.
- (39) Liu, X.; Atwater, M.; Wang, J.; Dai, Q.; Zou, J.; Brennan, J. P.; Huo, Q. A Study on Gold Nanoparticle Synthesis using Oleylamine as Both Reducing Agent and Protecting Ligand. *J. Nanosci. Nanotechnol.* **2007**, *7*, 3126–3133.
- (40) de la Hoz, A.; Diaz-Ortiz, A.; Moreno, A. Review of Non-Thermal Effects of Microwave Irradiation in Organic Synthesis. *J. Microwave Power Electromagn. Energy* **2007**, 41 (1), 45–66.
- (41) Johnston-Peck, A. C.; Wang, J.; Tracy, J. B. Synthesis and Structural and Magnetic Characterization of Ni (Core)/NiO (Shell) Nanoparticles. *ACS Nano* **2009**, *3*, 1077–1084.
- (42) Railsback, J. G.; Johnston-Peck, A. C.; Wang, J.; Tracy, J. B. Size-Dependent Nanoscale Kirkendall Effect During the Oxidation of Nickel Nanoparticles. *ACS Nano* **2010**, *4*, 1913–1920.
- (43) Herrero, M. A.; Kremsner, J. M.; Kappe, C. O. Nonthermal Microwave Effects Revisited: On the Importance of Internal Temperature Monitoring and Agitation in Microwave Chemistry. *J. Org. Chem.* **2008**, *73*, 36–47.
- (44) Link, S.; El-Sayed, M. A. Size and Temperature Dependence of the Plasmon Absorption of Colloidal Gold Nanoparticles. *J. Phys. Chem. B* **1999**, *103*, 4212–4217.
- (45) Haiss, W.; Thanh, N. T.; Aveyard, J.; Fernig, D. G. Determination of Size and Concentration of Gold Nanoparticles from UV- Vis Spectra. *Anal. Chem.* **2007**, *79*, 4215–4221.
- (46) Griffiths, D. J. Introduction to Electrodynamics. Prentice Hall: New Jersey, 1999.

(47) Abeledo, C. R.; Selwood, P. Temperature Dependence of Spontaneous Magnetization in Superparamagnetic Nickel. *J. Appl. Phys.* **1961**, 32, S229–S230.

- (48) Du, Y. W.; Xu, M. X.; Wu, J.; Shi, Y. B.; Lu, H. X.; Xue, R. H. Magnetic Properties of Ultrafine Nickel Particles. *J. Appl. Phys.* **1991**, 70, 5903–5905.
- (49) Gilbert, T.; Ekstein, H. Basis of the Domain Structure Variational Principle. Bull. Am. Phys. Soc. 1956, 1, 25.
- (50) Landau, L.; Lifshitz, E. On the Theory of the Dispersion of Magnetic Permeability in Ferromagnetic Bodies. *Phys. Z.* **1935**, *8*, 101–114.
- (51) Bødker, F.; Mørup, S.; Linderoth, S. Surface Effects in Metallic Iron Nanoparticles. *Phys. Rev. Lett.* **1994**, *72*, 282.
- (52) He, X.; Zhong, W.; Au, C.-T.; Du, Y. Size Dependence of the Magnetic Properties of Ni Nanoparticles Prepared by Thermal Decomposition Method. *Nanoscale Res. Lett.* **2013**, *8*, 446.
- (53) Mohamed, M. B.; AbouZeid, K. M.; Abdelsayed, V.; Aljarash, A. A.; El-Shall, M. S. Growth Mechanism of Anisotropic Gold Nanocrystals *via* Microwave Synthesis: Formation of Dioleamide by Gold Nanocatalysis. *ACS Nano* **2010**, *4*, 2766–2772.
- (54) Liu, Q.; Gao, M.-R.; Liu, Y.; Okasinski, J. S.; Ren, Y.; Sun, Y. Quantifying the Nucleation and Growth Kinetics of Microwave Nanochemistry Enabled by *In Situ* High-Energy X-Ray Scattering. *Nano Lett.* **2016**, *16*, 715–720.
- (55) Garnett, J. M. Colours in Metal Glasses, in Metallic Films, and in Metallic Solutions. II. *Philos. Trans. R. Soc., A* **1906**, 205, 237–288.
- (56) Mantese, J. V.; Micheli, A. L.; Dungan, D. F.; Geyer, R. G.; Baker-Jarvis, J.; Grosvenor, J. Applicability of Effective Medium Theory to Ferroelectric/Ferrimagnetic Composites with Composition and Frequency-Dependent Complex Permittivities and Permeabilities. *J. Appl. Phys.* 1996, 79, 1655–1660.